

Galactic winds and the Ly α forest

Vincent Desjacques¹, Adi Nusser¹, Martin G. Haehnelt²,
and Felix Stoehr³

¹*Physics Department and Space Research Institute, Technion-Haifa*

²*Institute of Astronomy, Madingley Rd, CB3-0HA, Cambridge, UK*

³*Max-Planck-Institut für Astrophysik, Karl-Schwarzschild-Str. 1, D-85740 Garching b. München, Germany*

30 October 2018

ABSTRACT

We study the effect of galactic outflows on the statistical properties of the Ly α forest and its correlation with galaxies. The winds are modelled as fully ionised spherical bubbles centered around the haloes in an N-body simulation of a Λ CDM model. The observed flux probability distribution and flux power spectrum limit the volume filling factor of bubbles to be less than 10%. We have compared the mean flux as a function of distance from haloes with the Adelberger *et al.* (ASSP) measurement. For a model of bubbles of constant size surrounding the most massive haloes, bubble radii of $\gtrsim 1.5 \text{ h}^{-1}\text{Mpc}$ are necessary to match the high transmissivity at separations $\leq 0.5 \text{ h}^{-1}\text{Mpc}$ but the increase of the transmissivity at small scales is more gradual than observed. The cosmic variance error due to the finite number of galaxies in the sample increases rapidly with decreasing separation. At separations $\leq 0.5 \text{ h}^{-1}\text{Mpc}$ our estimate of the cosmic variance error is $\Delta F \sim 0.3$, 30% higher than that of ASSP. The difficulty in matching the rise in the transmissivity at separations smaller than the size of the fully ionised bubbles surrounding the haloes is caused by residual absorption of neutral hydrogen lying physically outside the bubbles but having a redshift position similar to the haloes. The flux level is thus sensitive to the amplitude of the coherent velocity shear near halos and to a smaller extent to the amplitude of thermal motions. We find that the velocity shear increases with halo mass in the simulation. A model where LBGs are starbursts in small mass haloes matches the observations with smaller bubble radii than a model where massive haloes host the LBGs. If we account for the uncertainty in the redshift position of haloes, a starburst model with a bubble radius of $1 \text{ h}^{-1}\text{Mpc}$ and a volume filling factor of 2% is consistent with the ASSP measurements at the 1-1.5 σ level. If this model is correct the sharp rise of the transmissivity at separations $\leq 0.5 \text{ h}^{-1}\text{Mpc}$ in the ASSP sample is due to cosmic variance and is expected to become more moderate for a larger sample.

Key words: cosmology: theory – gravitation – dark matter – baryons – intergalactic medium

1 INTRODUCTION

Stellar feedback, in the form of ionising radiation and mechanical energy in galactic winds/outflows, plays an important role in determining the physical properties of galaxies and the Intergalactic Medium (IGM). The galactic contribution to the hydrogen ionising UV radiation may well exceed that of QSOs. Galactic superwinds regulate star formation, enrich the IGM with metals, and alter the dynamical and observational properties of the IGM close to galaxies.

Galactic winds are driven by the mechanical energy produced by supernova explosions of massive stars. They

have been studied extensively in nearby starburst galaxies (*e.g.* Heckman *et al.* 1990). The large velocity shifts between stellar and interstellar lines in the spectra of Lyman-break galaxies (LBGs) are strong evidence that galactic winds are also present in high-redshift galaxies (Pettini *et al.* 1998, 2000, Heckman *et al.* 2000). The inferred wind velocities are several hundred kms^{-1} , far above the sound speed of the IGM so that strong shocks are likely to be associated with these winds. These shocks will heat up, collisionally ionise, and sweep up the surrounding IGM near galaxies (Heckman 2000). Adelberger *et al.* (2003, hereafter ASSP) have analyzed a sample of high resolution QSO spectra with lines-

arXiv:astro-ph/0311209v2 2 Feb 2004

of-sight (LOS) passing very close to LBGs. They detected a significant decrease of the Ly α absorption near galaxies. As discussed by ASSP and Kollmeier et al. (2003) the increased UV flux close to LBGs falls short of explaining the decreased absorption by a factor of a few. The decreased absorption is thus taken as evidence for the existence of dilute and highly ionised gas bubbles caused by wind-driven shocks.

Initially a shock propagating in the IGM expands adiabatically. During this phase the gas encountered by the shock is heated and collisionally ionised to become part of a bubble of dilute and hot plasma. When radiative losses become important, a thin cool shell forms at the shock front. The shell is driven outwards by the hot low density inner plasma (e.g. Weaver *et al.* 1977, Ostriker & McKee 1988, Tegmark *et al.* 1993). Eventually the expansion of the plasma comes to a halt when pressure equilibrium with the surrounding IGM is reached. To explain the lack of H I close to the haloes, the bubble has to survive for a sufficiently long time. We defer the discussion of the conditions for the survival of the bubble to another paper. Here we assume that the bubbles are long-lived and study the implications of long-lived bubbles devoid of neutral hydrogen on QSO absorption spectra.

We will investigate how the correlation between the flux in the Ly α forest and the distance of the LOS to the closest galaxy depends on physical properties of the ionised bubbles around galaxies. For this purpose we use a N-body simulation of collisionless dark matter (DM). The basic observed properties of the Ly α forest can be reproduced with such simulations using a simple prescription that relates the distribution of gas and dark matter in the IGM (Hui & Gnedin 1997). With DM simulations it is possible to probe a wider dynamical range than with hydrodynamical simulations. This allows a better modelling of the statistical properties of the IGM-halo relation.

Measures of the halo-flux correlation, defined for example as the mean flux in the Ly α forest as a function of the distance to the nearest galaxies, are sensitive to the size of the bubbles. Absorption spectra probe the gas distribution in redshift space. Thermal motions and coherent peculiar velocities therefore strongly affect the halo-flux correlation at small separations (e.g. Kollmeier *et al.* 2003). Previous modelling of the impact of winds on the Ly α forest had difficulties to match the large decrease of the absorption measured by ASSP at comoving separation $s \leq 0.5 h^{-1} \text{Mpc}$ from the galaxies (Croft *et al.* 2002, Bruscoli *et al.* 2002, Theuns *et al.* 2002, Kollmeier *et al.* 2003). We will investigate here the role of peculiar velocities, thermal motions and the scaling of bubble size with halo mass in more detail. We will also perform a detailed assessment of the errors to obtain a more robust lower limit on the size and thus the volume filling factor of the bubbles.

The paper is organized as follows. In §2 we describe the model of the Ly α forest which we have used to calculate synthetic spectra from the DM simulations. In §3, we describe the simulation and the corresponding halo catalogs, compute three-dimensional flux maps of the simulation, and discuss the flux probability distribution function and power spectrum in the presence of winds. The main body of the paper are §4 and §5 where we study in detail the impact of galac-

tic winds on the halo-flux correlation and the corresponding observational errors. We conclude with a discussion of the results in §6.

2 THE LYMAN α FOREST AND THE MODERATE DENSITY IGM

The Ly α forest is now widely believed to originate from an undulating warm (10^4K) photoionized IGM. The Ly α optical depth in redshift space due to resonant scattering can be expressed as a convolution of the real space H I density along the line of sight with a Voigt profile \mathcal{H} (Gunn & Peterson 1965, Bahcall & Salpeter 1965),

$$\tau(w) = \frac{c\sigma_0}{H(z)} \times \int_{-\infty}^{+\infty} n_{\text{HI}}(x) \mathcal{H}[w - x - v_p(x), b(x)] dx. \quad (1)$$

where $\sigma_0 = 4.45 \times 10^{-18} \text{ cm}^2$ is the effective cross-section for resonant line scattering and $H(z)$ is the Hubble constant at redshift z , x is the real space coordinate, $v_p(x)$ is the line of sight component of the H I peculiar velocity field, \mathcal{H} is the Voigt profile, and $b(x)$ is the Doppler parameter due to thermal/turbulent broadening. For thermal broadening $b(\mathbf{x}) = 13 \left(\frac{T(\mathbf{x})}{10^4 \text{K}} \right)^{1/2} \text{ km s}^{-1}$, where T is the temperature of the gas.

Both x and w are measured in km s^{-1} . The Voigt profile is normalized such that $\int \mathcal{H} = 1$ and can be approximated by a Gaussian for moderate optical depths, $\mathcal{H} = 1/(\pi^{1/2}b) \times \exp\{-[\omega - x - v_p(x)]^2/b^2\}$.

The normalized flux obtained by “continuum fitting” of the observed spectrum is related to the optical depth along the line of sight as,

$$F(w) \equiv I_{\text{obs}}(w)/I_{\text{cont}} = e^{-\tau(w)}, \quad (2)$$

where τ is the optical depth, w is the redshift space coordinate along the line of sight, I_{obs} is the observed flux and I_{cont} is the flux emitted from the source (quasar) that would be observed in the absence of any intervening material.

On scales larger than a filtering scale which is related to the Jeans scale, x_J , the IGM traces the DM distribution very well. For moderate overdensities the balance between adiabatic cooling and photo-heating of the expanding IGM establishes power-law relations between temperature, neutral hydrogen density and total gas density (Katz *et al.* 1996, Hui & Gnedin 1997, Theuns *et al.* 1998),

$$T_g \propto \rho_g^\beta \quad \text{and} \quad n_{\text{HI}} \propto \rho_g^\alpha, \quad (3)$$

where the parameter β is in the range $0 - 0.62$, $\alpha = 2 - 0.7\beta$, and ρ_g and T_g are the density and temperature of the gas, respectively.

On scales smaller than the Jeans scale pressure dominates over gravity. The gas pressure smoothes the gas distribution compared to the distribution of collisionless dark

Table 1. The principle parameters of the N-body simulation. The number of particles, N , and the particle mass, m , in the high resolution region are also listed.

Ω_m	Ω_Λ	h	σ_8	N	$m/[10^8 M_\odot/h]$
0.3	0.7	0.7	0.9	12067979	9.52

matter (e.g. Theuns, Schaye & Haehnelt 2000). We thus assume that $\rho_g(\mathbf{x}) \propto \rho_{\text{dm}}^s(\mathbf{x})$, where $\rho_{\text{dm}}^s(\mathbf{x})$ is the dark matter density smoothed in a way that mimics the pressure effects. We adopt the smoothing used in SPH simulations (e.g. Springel, Yoshida & White 2001) to estimate the gas density from the dark matter particle distribution. The HI density n_{HI} and the smoothed dark matter field ρ_{dm}^s are then related as

$$n_{\text{HI}}(\mathbf{x}) = \hat{n}_{\text{HI}} \left[\frac{\rho_{\text{dm}}^s(\mathbf{x})}{\bar{\rho}_{\text{dm}}^s} \right]^\alpha, \quad (4)$$

where $\bar{\rho}_{\text{dm}}^s$ is the (volume) average of ρ_{dm}^s , and \hat{n}_{HI} is the HI density at $\rho_{\text{dm}}^s = \bar{\rho}_{\text{dm}}^s$.

3 SIMULATING GALAXIES AND THE FLUX DISTRIBUTION

3.1 The DM simulation

One of our main goals is to assess the error in the observed galaxy flux correlation. This requires a simulation large enough to contain a substantial number of DM haloes which can be identified as hosts of LBGs. At the same time the simulation should still reproduce typical absorption systems. This favours the use of a DM simulation for which a larger dynamical range can be achieved rather than a computationally more expensive hydrodynamical simulation. We use a Λ CDM simulation run with the N-body code GADGET (Springel, Yoshida & White 2001). The cosmological parameters are listed in Table 1. It is part of a series of simulations of increasingly higher resolution which zoom in on a spherical region of initial comoving radius $26 h^{-1}\text{Mpc}$ selected from a simulation with box size $479 h^{-1}\text{Mpc}$ (cf. Stoehr *et al.* 2002). The inner region of the simulation has thus higher resolution than the outer regions. We only use the particle distribution inside a box of size $L = 30 h^{-1}\text{Mpc}$ which belongs to the spherical region of high resolution. The particle mass in this high-resolution region is $m = 9.52 \times 10^8 M_\odot/h$ (cf. Table 1). The large volume makes the simulation well suited for a direct comparison with the observed galaxy-flux correlation. We use a redshift output $z = 3$ to facilitate a comparison with the ASSP measurements.

3.2 DM haloes as host of LBGs

We aim at extracting halo catalogs with statistical properties similar to those of observed Lyman-break galaxies (LBGs). However, the relation between LBG and DM haloes

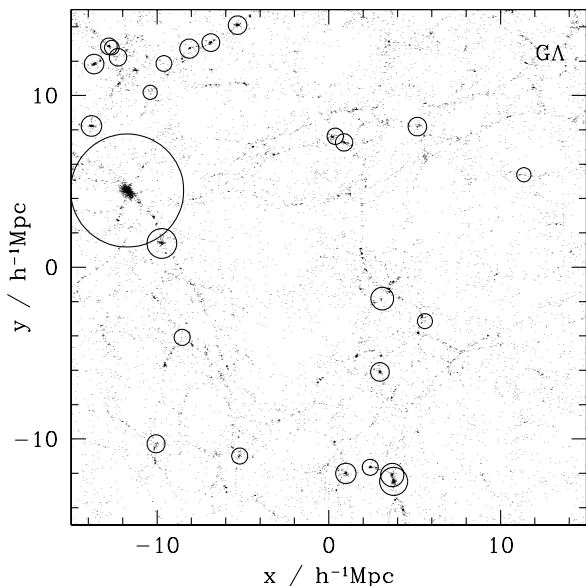
is still somewhat uncertain. When LBGs were first discovered, a simple picture was advocated in which the mass of the DM haloes hosting the LBGs scales approximately linearly with the luminosity of LBGs, LBGs are long-lived and each DM halo hosts one LBG (e.g. Steidel *et al.* 1996; Adelberger *et al.* 1998, Bagla 1998; Haehnelt, Natarajan & Rees 1998). In this “massive-halo” scenario the masses of the host haloes are rather large, $M \gtrsim 10^{12} M_\odot/h$, and the high-redshift LBGs are the progenitors of today’s massive and luminous galaxies. The rather slow decrease of the LBG space density with increasing redshift motivated an alternative picture, where most of the observed LBGs are interacting starburst galaxies in the process of assembling (e.g. Lowenthal *et al.* 1997, Trager *et al.* 1997, Kolatt *et al.* 1999, Somerville *et al.* 2001). We will call this scenario the “starburst” picture in the following. It predicts that most of the observed LBGs are hosted by haloes of smaller mass $M \sim 10^{11} M_\odot/h$, which will eventually merge to form more typical galaxies at $z \simeq 0$. Both scenarios predict similar clustering properties and cannot be ruled out based on the available clustering data (e.g. Wechsler *et al.* 2001). Direct observational constraints on the masses of LBGs are also still rather weak. Studies of rest-frame optical nebular emission lines imply halo masses in the range $10^{10} - 10^{11} M_\odot/h$ (e.g. Pettini *et al.* 1998), while near-infrared imaging surveys combined with stellar population synthesis models and extinction yield virial masses of $M \sim 10^{11} - 10^{12} M_\odot/h$ (e.g. Shapley *et al.* 2001). We will here first adopt the massive halo picture *i.e.* we assume that a dark matter halo contains only one LBG (e.g. Adelberger *et al.* 1998) and pick a minimum mass M_{min} such that the number density of haloes $M \geq M_{\text{min}}$ in the simulation is similar to the observed number density of high-redshift LBGs. In Section §5.4 we will discuss what happens if we relax these assumptions.

DM haloes were identified with a Friends-of-Friends group finding algorithm. Only groups containing at least 20 dark matter (DM) particles were classified as haloes. Since the DM particle mass is $9.52 \times 10^8 M_\odot/h$, the minimum halo mass is about $2 \times 10^{10} M_\odot/h$. Figure 1 shows a slice of thickness $\Delta h = 0.21 h^{-1}\text{Mpc}$ at $z = 3$ in the simulation. The centers of the open circles show the location of haloes with $M \geq 5 \times 10^{10} M_\odot/h$. The radii of the circles are proportional to their masses.

In the simulation the number density of haloes with $M \geq 10^{11} M_\odot/h$ is about $0.04 h^2\text{Mpc}^{-3}$, whereas for haloes with $M \geq 10^{12} M_\odot/h$ it is about $2 \times 10^{-3} h^2\text{Mpc}^{-3}$ (cf. Table 2). We have chosen $M_{\text{min}} = 5 \times 10^{11} M_\odot/h$ as our reference value but have also studied alternative choices. The corresponding number density is $4 \times 10^{-3} h^2\text{Mpc}^{-3}$, which is about the number density of LBGs as determined for a Λ CDM cosmology at $z = 3$ from high-redshift surveys with limiting magnitude $25 \leq \mathcal{R} \leq 27$ (Giavalisco & Dickinson 2001). It should be noted that the halo cumulative function $n_h(m_h)$ as shown in Table 2 is consistent with a Sheth-Tormen mass function computed for a Λ CDM Universe with identical parameters as our simulation (cf. Table 1).

Table 2. Number densities of haloes with mass greater than the listed four values.

$m_h/[10^{10} M_\odot/h]$	5	10	50	10^2
$n_h(> m_h)/[10^{-3} h^3 \text{Mpc}^{-3}]$	81	36	3.9	1.6

**Figure 1.** The particle distribution at $z = 3$ in a slice of thickness $\Delta h = 0.21 h^{-1} \text{Mpc}$. Haloes with masses $M \geq 5 \times 10^{10} M_\odot/h$ are represented by the open circles with radii proportional to their masses.

3.3 Calculating synthetic spectra from the dark matter distribution

3.3.1 From density to flux

The HI and the flux distributions are calculated from the DM distribution which was smoothed with a SPH kernel containing 20 particles within the smoothing length. The smoothed DM density and velocity fields, ρ_{dm}^s and \mathbf{v}_{dm}^s , were interpolated for randomly chosen LOS through the simulation box. The pixel size of the spectra is $\Delta = 60 h^{-1} \text{kpc}$ and the comoving length $30 h^{-1} \text{Mpc}$. From the density and velocity fields along the LOS we computed the optical depth as a function of the redshift space coordinate $w = x + v_p$, where v_p is the component of \mathbf{v}_{dm}^s in the line of sight direction. Eq. (1) then takes the following discrete form,

$$\tau(w_i) = \mathcal{A}(z) \Delta \sum_j [\rho_{\text{dm}}^s(x_j)]^\alpha \mathcal{H}_{ij}, \quad (5)$$

where $\mathcal{A} = c\sigma_0 n_{\text{HI}}(\bar{\rho}_{\text{dm}}^s)/H(z)$ and we assume that ρ_{dm}^s is normalized such that its mean is unity and $\mathcal{H}_{ij} = \mathcal{H}[w_i - x_j - v_p(x_j), b(x_j)]$ is a normalized Gaussian profile.

3.3.2 The temperature distribution

As we are using a DM simulation we still have to specify a temperature. For this we use the fact that temperature and density are tightly coupled. At moderate densities a simple power-law relation holds, $T_g \sim \rho_{\text{dm}}^s{}^\beta$ (cf. eq 3). In high-density regions, line cooling is efficient and the gas rapidly cools to $T \sim 10^4 \text{K}$ (e.g. Theuns *et al.* 1998, Davé *et al.* 1999). We will thus take the following relation between temperature and density

$$T_g = \begin{cases} \hat{T} \left(\frac{\rho_{\text{dm}}^s}{\bar{\rho}_{\text{dm}}^s} \right)^\beta & \frac{\delta\rho}{\rho} \leq 50 \\ 10^4 \text{K} & \frac{\delta\rho}{\rho} > 50 \end{cases} \quad (6)$$

In the high-density regions where shock heating is important this is only a very crude approximation of the $T - \rho$ diagram of hydrodynamical simulation (Theuns *et al.* 1998, Davé *et al.* 1999, Croft *et al.* 2002). However, it is mainly the moderate density regions which are responsible for the Ly α forest. Eq. (6) should thus be sufficient for our purposes. The gas temperature \hat{T} at fixed overdensity is expected to evolve with redshift. Schaye *et al.* 2000 and Theuns *et al.* 2002 claim to have detected a peak at $z = 3$ with decreasing temperature towards lower and higher redshifts. Note that we have ignored a possible redshift dependence and have assumed $\hat{T} = 15000 \text{K} \simeq 10^{4.2} \text{K}$ independent of redshift.

3.3.3 The effect of wind bubbles

We have adopted a very simple model for the effect of wind bubbles. We simply assume that shocks produce long-lived *fully ionised* spherical bubbles around galaxies (see appendix A for a discussion of the physical properties of expanding wind bubbles). We assume that the neutral hydrogen HI density is zero in a spherical region of radius r_w centered on the DM haloes which we have chosen to identify as LBGs. Note that this simple model has also been discussed in Croft *et al.* (2002), Kollmeier *et al.* 2003 (2003a,2003b) and Weinberg *et al.* (2003). In the simulation, most of the haloes lie along filaments, or at the intersection of filaments, and the gas distribution around the haloes is often anisotropic on the scale of galactic winds (e.g. Croft *et al.* 2002, Springel & Hernquist 2003). Theuns *et al.* (2002) have also shown that winds propagate more easily into the low density IGM than in the filaments, giving rise to highly ionised regions which are generally not spherical. It should thus be kept in mind that our assumption of a spherical wind bubble will only be a reasonable approximation for strong isotropic winds. Furthermore the bubbles do not necessarily live longer than a Hubble time. A discussion of the physical properties of shocks in the IGM can be found in Appendix A3.

3.3.4 Properties of the synthetic spectra

Once we have smoothed the dark matter density ρ_{dm}^s , the flux distribution depends only on \mathcal{A} and α and the size distribution of wind bubbles. We have assumed $\alpha = 1.6$ and constrain \mathcal{A} from a random sample of 500 lines of sight of

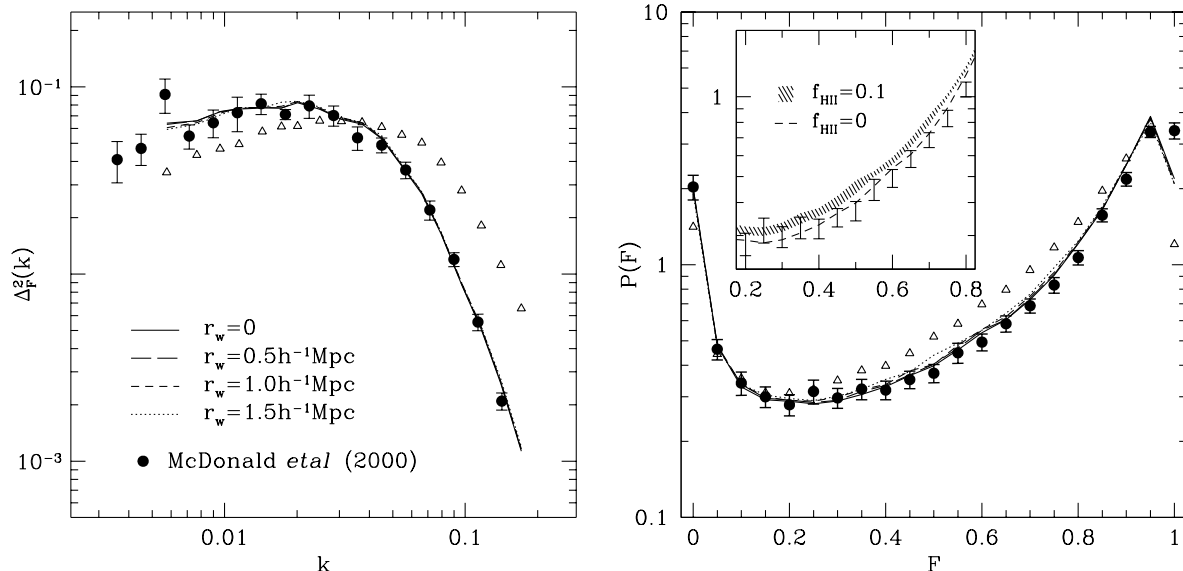


Figure 2. The flux power spectrum (left panel) and PDF (right panel) at $z = 3$ with wind bubbles of radius $r_w = 0$ (solid line), $r_w = 0.5$ (long-dashed line), $r_w = 1.0$ (short-dashed line) and $r_w = 1.5 \text{ h}^{-1} \text{ Mpc}$ (dotted line). The results are compared to the observations of McDonald *et al.* (2000), shown as filled symbols. The triangles are the various volume averaged statistics in real space. The small plot in the right panel shows the PDF for filling factors of zero and ten percent (cf. text). The wavenumber k is in unit of km s^{-1} .

comoving length $L = 30 \text{ h}^{-1} \text{ Mpc}$ by demanding that the mean flux $\langle F \rangle$ is equal to the observed value $\langle F \rangle = 0.67$ (Rauch *et al.* 1997, McDonald *et al.* 2000). The effect of varying the assumed size distribution of wind bubbles are discussed in the following sections. The spectral resolution is $\Delta v \simeq 6 \text{ km s}^{-1}$, somewhat smaller than in the ASSP data, where it is $\Delta v \lesssim 10 \text{ km s}^{-1}$. Note that the mean inter-particle distance in the simulation is $\sim 0.2 \text{ h}^{-1} \text{ Mpc}$. This is sufficient to resolve \bar{F} on a scale $r \sim 0.25 \text{ h}^{-1} \text{ Mpc} \sim 27 \text{ km s}^{-1}$ as in the observations, but is somewhat too low to resolve all the features of the Ly α absorption lines (e.g. Theuns *et al.* 1998, Bryan *et al.* 1999). We also add noise with signal-to-noise $S/N=50$ per pixel of width $\Delta\pi = 2.5 \text{ km s}^{-1}$.

3.4 Volume averaged statistics: The flux PDF and the flux power spectrum

We will first investigate some basic flux statistics of our synthetic spectra to check if they are a reasonable representation of observed spectra and to study the effect of the wind bubbles. We begin with the flux probability distribution function (PDF) defined as the fraction of the volume of the IGM which has a flux value within a certain range. The right panel of Fig. 2 compares the flux PDF at $z = 3$ for wind bubbles with different radii r_w . The filled circles show the observed PDF from McDonald *et al.* 2000, while the solid, long-dashed, short-dashed and dotted curves correspond to $r_w = 0$ (i.e., no wind), 0.5, 1 and 1.5 $\text{h}^{-1} \text{ Mpc}$, respectively. Following McDonald *et al.* (2000) we use 21 bins of width $\Delta F = 0.05$ to compute the flux PDF. The PDF of spectra without wind bubbles (solid curve) agrees very well with the PDF of the observed spectra (filled circles). Including wind bubbles with $r_w = 0.5 \text{ h}^{-1} \text{ Mpc}$ has no

significant effect on the flux PDF, and even when r_w is as large as $1.5 \text{ h}^{-1} \text{ Mpc}$ there is only a slight discrepancy with the flux PDF of the observed spectra in saturated regions with $F \sim 0$. The small effect of the wind bubbles is due to their small volume filling factor f_{HII} , which is about 5% for the model with $r_w = 1.5 \text{ h}^{-1} \text{ Mpc}$. This is consistent with the findings of Theuns *et al.* (2002) and Weinberg *et al.* (2003).

We can place an upper bound on the volume filling factor, f_{HII} , of bubbles by demanding a good match between the simulated and observed PDFs. We have computed the flux PDF for several bubbles radii for which f_{HII} is in the range 0.01-0.5. To account for the uncertainty in the mass of LBGs, we performed three computations for each f_{HII} : we selected DM haloes with mass M larger than 5×10^{10} , 10^{11} and $5 \times 10^{11} M_\odot/h$, and adjusted r_w which gives the desired f_{HII} . We find that independent of halo mass, a filling factor $f_{\text{HII}} \gtrsim 0.1$ yields a poor match to the observations, especially in the range $0.2 \lesssim F \lesssim 0.8$, as shown in the small plot inside the right panel of Fig. 2.

In the left panel of Fig. 2 we show the dimensionless one-dimensional flux power $\Delta_F^2(k)$ as a function of k (in km s^{-1}), defined as

$$\Delta_F^2(k) = \frac{L}{\pi} k |\delta_k|^2, \quad (7)$$

where δ_k is the Fourier Transform of the flux contrast $(F/\langle F \rangle - 1)$. The flux power spectrum was calculated with a FFT routine from 500 synthetic spectra. Note that our simulation box and therefore the spectra are not periodic which may lead to small artifacts at small scales. The flux power of our synthetic spectra and that of the observed spectra obtained by McDonald *et al.* (2000) also agree very well. Bubbles of size as large as $r_w = 1 \text{ h}^{-1} \text{ Mpc}$ have again a very

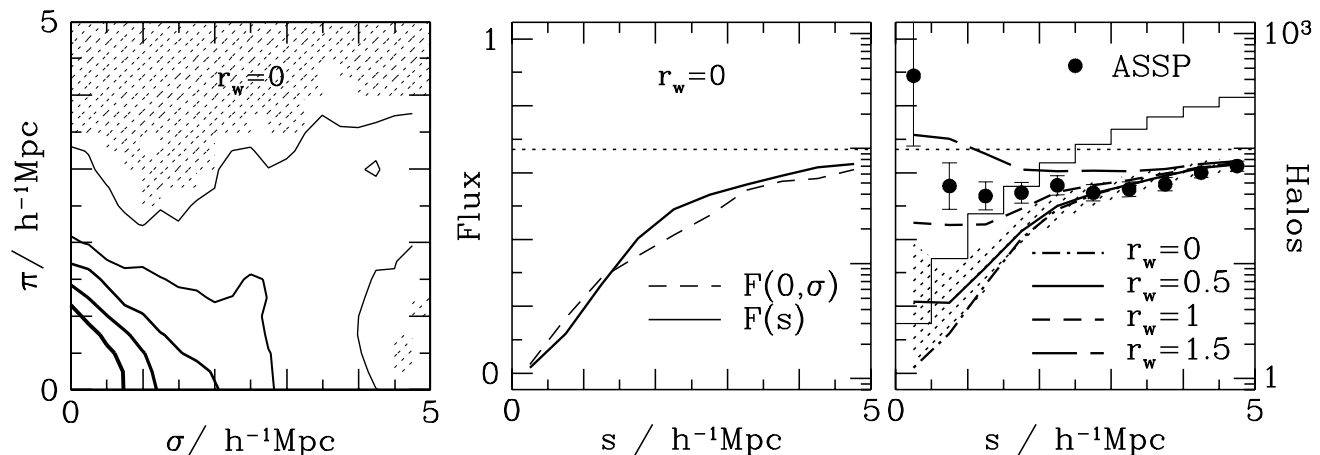


Figure 3. *Left panel*: Contours of the 2D conditional flux $\bar{F}(\pi, \sigma)$ around the nearest LBG-size halo in the simulation at $z = 3$ (cf. text). The (comoving) bin size is $\Delta s = 0.25 \text{ h}^{-1}\text{Mpc}$. The shaded pixels have a flux within 0.05 of the mean flux level, $\langle F \rangle = 0.67$. *Middle panel*: The mean transmitted flux $\bar{F}(s)$ at distance $|\mathbf{s}| = \sqrt{\pi^2 + \sigma^2}$, compared to $\bar{F}(0, \sigma)$. The dotted curve shows the mean flux level. *Right panel*: The mean transmitted flux, when LBG-size haloes were surrounded by wind bubbles with radius $r_w = 0.5$, $r_w = 1 \text{ h}^{-1}\text{Mpc}$ and $r_w = 1.5 \text{ h}^{-1}\text{Mpc}$, respectively, as indicated in the figure. The Adelberger *et al.* (2003) measurements are shown as filled symbols. The shaded area is the 1σ error for the model $r_w = 0.5 \text{ h}^{-1}\text{Mpc}$, and was computed from $N(< s)$ shown as an histogram (right axis).

small effect due to their small volume filling factor (e.g. Croft *et al.* 2002, Weinberg *et al.* 2003).

To demonstrate the role of peculiar velocities, the triangles in Fig. 2 show the flux PDF and the power spectrum in real space for $r_w = 0$ obtained by setting the peculiar velocities and thermal motions to zero. The real space flux PDF and power spectrum significantly deviate from the observations.

4 PROBING CORRELATIONS BETWEEN FLUX AND HALOES/LBGs

4.1 Statistical measures of the flux-halo correlation

There is a variety of statistical measures which can describe the correlation between the flux along a LOS and nearby galaxies. Here we will focus on the conditional flux function, \bar{F} . \bar{F} is the mean flux at real-space distance $|\mathbf{s}| = s$ to the next halo,

$$\bar{F}(\mathbf{s}) = \frac{1}{N_h} \sum F(\mathbf{s}|\text{halo}), \quad (8)$$

where N_h is the total number of haloes, $F(\mathbf{s}|\text{halo})$ is the value of the flux at a distance s from the nearest halo. Note that we use the position of the haloes which we identify as host haloes of LBGs as a proxy for the galaxy position. Results will thus depend on how this identification is done and we will later explore several possibilities. The summation is performed over a representative sample of haloes. The function \bar{F} can be expressed in terms of the unconditional two-point correlation ξ_{hf} as

$$\bar{F}(\mathbf{s}) = \langle F \rangle [1 + \xi_{\text{hf}}(\mathbf{s})]. \quad (9)$$

Relation (9) also holds in redshift space. In the following π and σ are the coordinates of \mathbf{s} parallel and perpendicular to the LOS, respectively.

4.2 Calculating the mean flux as function of the distance to the nearest halo

For the numerical simulation we know the full 3-dimensional flux field. We could therefore estimate $\bar{F}(s)$ from the transverse correlation $\bar{F}(\pi = 0, \sigma)$. However, real observation will sample the flux field $\bar{F}(\mathbf{s})$ more sparsely. ASSP have therefore estimated $\bar{F}(s)$ from the averaged 2D halo flux correlation function ξ_{hf} using eq. (9) in order to maximize the signal. We proceed as ASSP do and calculate $\bar{F}(s)$ as follows. We first pick a LOS direction. We then produce an ensemble of spectra along this direction with random offsets perpendicular to the chosen direction. For each pair of halo/spectrum we determine the flux $\bar{F}(\pi, \sigma)$, the distance σ at the point of closest approach, and the distance π between the halo and a given pixel of the spectrum. This process is repeated for an ensemble of randomly chosen LOS directions. We then obtain $\bar{F}(s)$ by annular averaging $\bar{F}(\pi, \sigma)$, and binning in bins of comoving size Δs . We further average over all haloes and LOS. In the left panel of Fig. 3 we plot the full 2D distribution of the average flux $\bar{F}(\pi, \sigma)$ around haloes assumed to host LBGs. The haloes were assumed to have no galactic wind bubbles. The bin size is $0.25 \text{ h}^{-1}\text{Mpc}$, twice smaller than that we use for \bar{F} . The shaded area shows bins for which \bar{F} is within 0.05 from the mean flux $\langle F \rangle$. Contours are for flux levels increasing from 0.2 to 0.6 with decreasing line width. The contours are compressed along the line of sight as a result of the peculiar and thermal motions of the

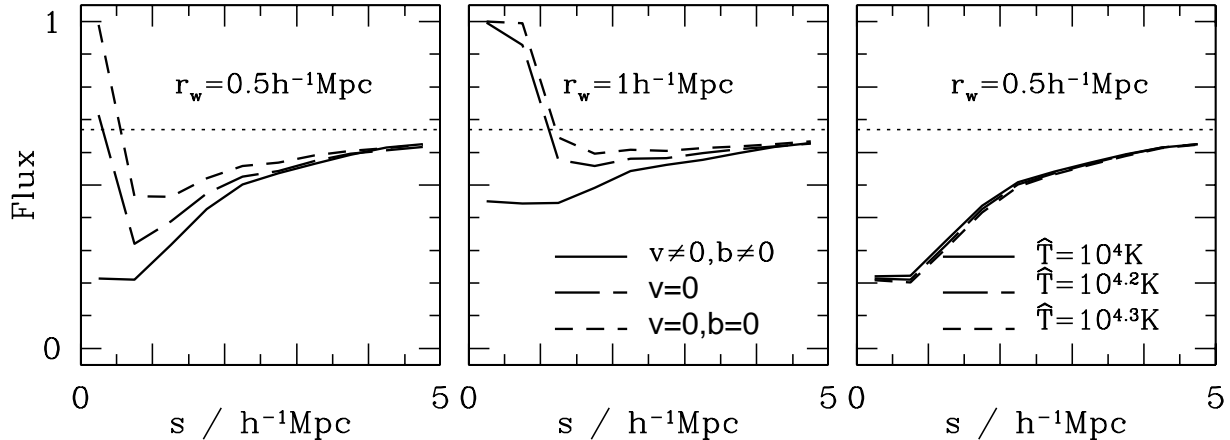


Figure 4. *Left and Middle panels* : The transmitted flux in redshift space (solid), with gas and halo velocities set to zero but with non-zero Doppler parameter b (long-dashed), and with velocities and b set to zero (short-dashed). *Panel to the right* : The transmitted flux as a function of the mean IGM temperature \hat{T} as indicated on the figure. In each panel the horizontal dotted line shows the mean flux level, $\langle F \rangle = 0.67$.

gas. At small separation the transmissivity is much smaller than the mean due to the increased density near haloes.

Redshift distortions cause $\bar{F}(s)$ (as computed in ASSP) to be different from the transverse correlation $\bar{F}(\pi = 0, \sigma)$. This can be seen in the middle panel of Fig. 3. The effect is important for $s \sim 1 - 3 \text{ h}^{-1}\text{Mpc}$. Note that previous work compared also the ASSP measurements with $\bar{F}(s)$ obtained from numerical simulations (e.g. Croft *et al.* 2002, Kollmeier *et al.* 2003, Bruscoli *et al.* 2003).

4.3 Estimating errors due to sparse sampling

The sample of ASSP contains 431 galaxies in 7 fields containing a QSO (one field contains two QSOs). At large scales ($> \text{a few Mpc}$) the number of galaxy LOS pairs is reasonably large. However at small scales the number of available galaxies becomes very small. There are *e.g.* only 3 galaxies within a transverse separation of $0.5 \text{ h}^{-1}\text{Mpc}$ to the line-of-sight to a QSO. Obviously Poisson errors will then be large and estimating these errors is thus important. In the following we use the term *cosmic variance* to describe the error resulting from the finite number of galaxies and QSO spectra. At small scales cosmic variance is the dominant source of error. Other sources of errors also affect the calculation of \bar{F} , mainly the uncertainty of the mean flux $\langle F \rangle$, and the redshift position of the galaxies. These errors will be discussed in Section §5.3.

About one LOS from a bright QSO is expected to pass through a region of angular dimensions comparable to that of our simulation box at $z = 3$. However, the correlation length of the flux is around a few h^{-1}Mpc . There will thus be about a hundred LOS through the simulation box which represent independent flux measurements. We therefore estimate the cosmic variance error as follows from the simu-

lation. For each separation bin of width $\Delta s = 0.5 \text{ h}^{-1}\text{Mpc}$ we perform Monte-Carlo realizations of $\bar{F}(s)$, where $\bar{F}(s)$ is averaged over the halo/spectrum pairs lying in the given bin. The cosmic variance error is then the 1σ scatter around $\bar{F}(s)$. The error of $\bar{F}(s)$ depends on the total number of galaxies/haloes with separation s . A sample of about 40 LOS through our simulation box gives a cumulative halo function $N(< s)$ close to the cumulative galaxy function N_{LFG} of the ASSP sample for separation $s \leq 1 \text{ h}^{-1}\text{Mpc}$. Note also that the number of haloes with $M > M_{\text{min}}$ in the simulation is only about 110. This means that we severely oversample the halo catalog when we estimate the cosmic variance on large scales. However, at the small scales in which we are mainly interested this should have little effect.

5 THE HALO FLUX CORRELATION OF OBSERVED AND SIMULATED SPECTRA

5.1 Wind bubbles and the halo flux correlation

We first explore the shape of \bar{F} assuming that all wind bubbles have the same radius, r_w , independent of the halo mass that they surround. In the right panel of Fig. 3 we plot \bar{F} for haloes with mass $M \geq M_{\text{min}}$. We show curves for $r_w = 0.5, 1$ and $1.5 \text{ h}^{-1}\text{Mpc}$ as indicated in the figure. The corresponding filling factors are $f_{\text{HII}} \sim 0.2\%$, $\sim 1.6\%$ and $\sim 5.3\%$ respectively, small enough to ensure that the flux PDF, the power spectrum and the line distribution of the Ly α forest are not affected. The dashed-dotted curve corresponds to \bar{F} in the absence of outflows. The filled symbols show the observed correlation as given in ASSP. The shaded area shows the cosmic variance error, and is calculated (cf. Section §4.3) from the cumulative halo distribution $N(< s)$ also shown as a histogram in the right panel of Fig. 3 (right axis). The cosmic variance error is only shown for $r_w = 0.5 \text{ h}^{-1}\text{Mpc}$.

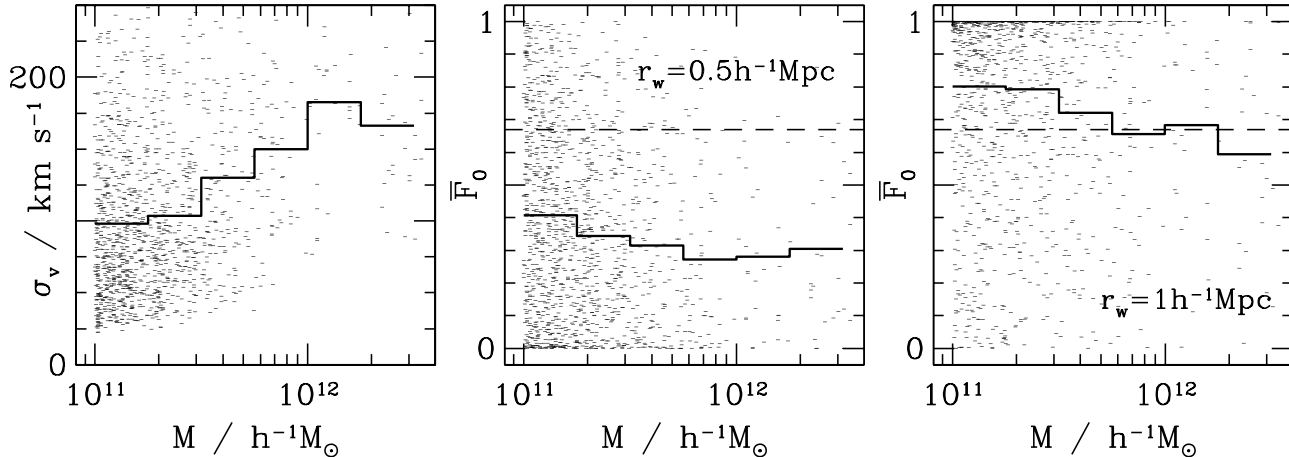


Figure 5. *left panel* : The velocity dispersion along the line of sight σ_v near haloes of mass $M \geq 10^{11} M_\odot/h$. The solid line is σ_v averaged over bins of size $\Delta \log M = 0.25$. *Middle and right panels* : the transmitted flux at separation $s \leq 0.5 h^{-1} \text{Mpc}$, \bar{F}_0 , as a function of M . The horizontal dashed line is $\langle F \rangle = 0.67$.

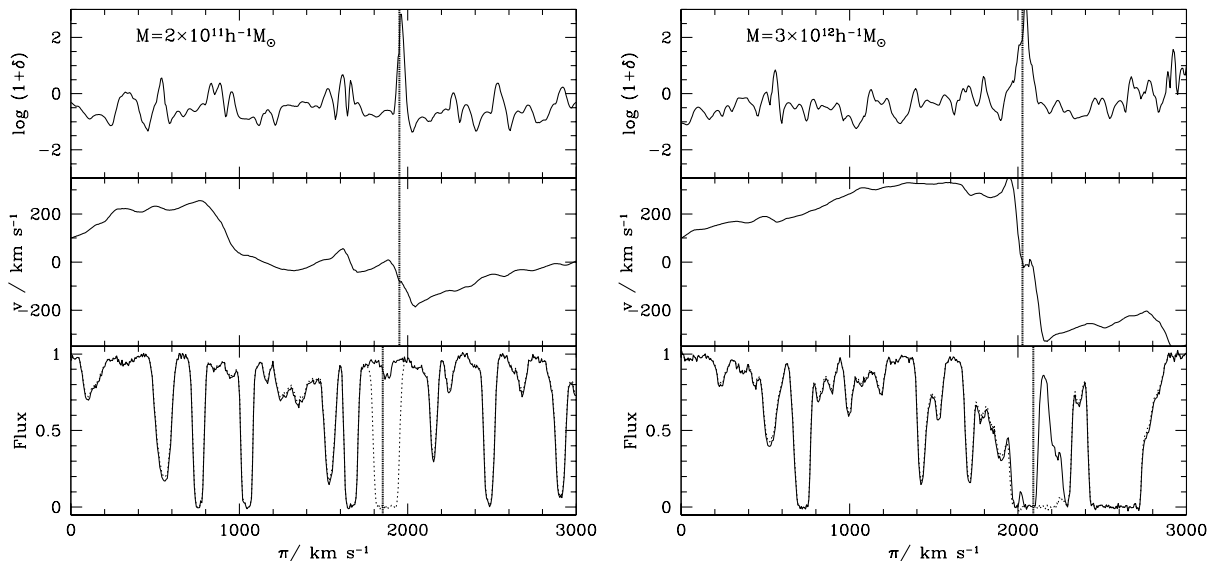


Figure 6. One-dimensional gas density, velocity (real space) and transmitted flux (redshift space) along two lines of sight extracted from simulation at $z = 3$, running through the centers of haloes with mass $M = 2 \times 10^{11}$ (left panel) and $M = 3 \times 10^{12} M_\odot/h$ (right panel). The halo positions along the line of sight are shown by vertical lines. The transmitted flux is computed with winds (solid line) and without winds (dotted line). The bubble radius is $r_w = 0.5 h^{-1} \text{Mpc}$.

The trend of decreasing mean flux with decreasing distance to the next galaxy in the observations is well reproduced by the numerical simulations. At small separation this trend is inverted if the wind bubbles are included. As Kollmeier et al. (2003a, 2003b) we find that the strong increase of the mean flux level at $s \gtrsim 0.5 h^{-1} \text{Mpc}$, is only reproduced for bubbles with size as large as $r_w \gtrsim 1.5 h^{-1} \text{Mpc}$. We thus confirm the difficulty of other authors to reproduce the mean flux at small separation unless rather large bubbles are included. Bubbles of this size are, however, difficult to

explain even with very efficient galactic superwinds (Croft et al. 2002).

There are thus two possibilities: the simple model of spherical wind bubbles of constant size around massive haloes does not describe the effect of winds of observed galaxies properly or the observed strong increase of the flux level in the ASSP is a statistical fluke. We will explore both possibilities in the following sections in more detail.

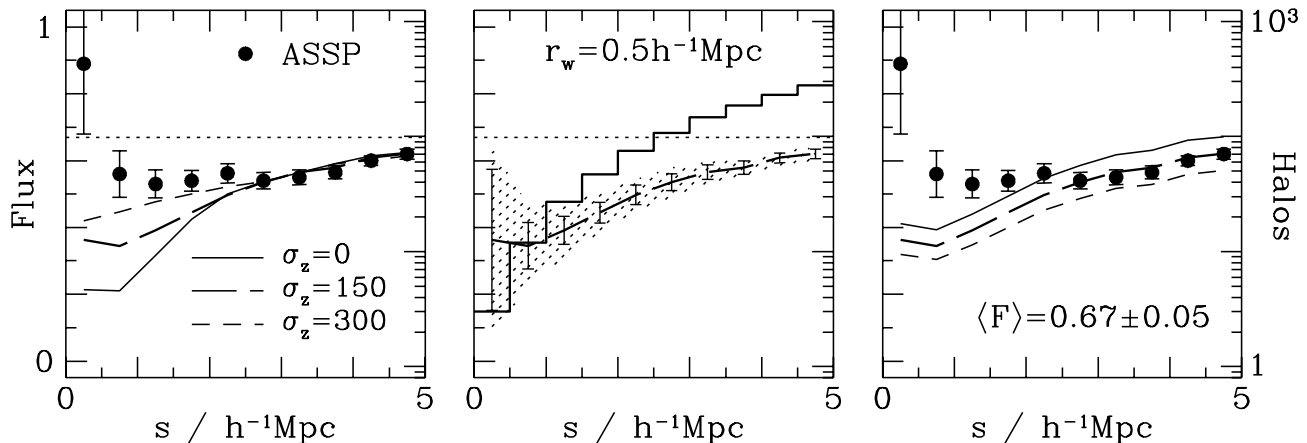


Figure 7. *Left panel* : The transmitted flux \bar{F} for bubbles of size $r_w = 0.5 h^{-1} \text{Mpc}$ after adding a Gaussian deviate of variance $\sigma_z = 0$, $\sigma_z = 150$ and 300 km s^{-1} to the LOS halo position. *Middle panel* : The cumulative halo function (histogram) and the 1σ error (shaded area) for the model with $\sigma_z = 150 \text{ km s}^{-1}$. *Right panel* : The transmitted flux with a mean flux level $\langle F \rangle = 0.62, 0.67$ and 0.72 . The filled symbols are the measurements by Adelberger *et al.* .

5.2 The effect of peculiar motions and thermal broadening

Kollmeier *et al.* (2002) have pointed out that the peculiar velocities of matter infalling onto the galaxy/DM halo expected from hierarchical structure formation should have a strong influence on $\bar{F}(s)$ at small separations. In Fig. 4 we investigate the effect of coherent small-scale peculiar velocities and thermal velocities. In the left and middle panel we show $\bar{F}(s)$ with and without peculiar and thermal velocities for wind bubbles of size $r_w = 0.5 h^{-1} \text{Mpc}$ and $r_w = 1 h^{-1} \text{Mpc}$, respectively. Without peculiar velocity the increase of the mean flux at small separation is much more pronounced. This is easy to understand. In redshift space the velocity shear of the infalling surrounding material fills in the cavity which is caused by the fully ionised wind bubble in real space. For the smaller bubble size such an effect is also visible for the thermal velocities alone. Neutral hydrogen HI lying at the boundary of the ionised bubbles leads to significant Ly α absorption at the redshift halo position when the ratio b/r_w is large enough. The peculiar velocity will, however, always dominate over the effect of thermal velocities. This can be seen in the right panel where we have scaled the temperature of the gas up and down. This has very little effect on $\bar{F}(s)$ calculated with peculiar velocities even for the smaller bubble size. We have also computed $\bar{F}(s)$ for various values of the density threshold in eq. (6). We found only small differences for $10 \lesssim \delta\rho/\rho \lesssim 100$. Such overdensities occur typically within $\lesssim 0.2 h^{-1} \text{Mpc}$ (comoving) from the halo (Kollmeier *et al.* 2003) which is smaller than the bubble radii considered here. Note that the good agreement of the flux PDF of the synthetic spectra with the McDonald *et al.* (2000) data found in section 3 disappeared if peculiar velocities were set to zero. This indicates that our simulations have similar peculiar velocities as the gas responsible for the observed absorption – at least in a volume-averaged sense.

In the left panel of Fig. 5 the black dots show the velocity dispersion for haloes of mass M . For each DM halo the velocity shear σ_v along the line of sight was calculated along three perpendicular LOS directions for an interval $\Delta\pi = 2 h^{-1} \text{Mpc}$ centered on the halo position. The histogram shows the mean velocity dispersion averaged over bins with $\Delta \log M = 0.25$. The velocity shear clearly increases with halo mass. This trend is present for a range of $\Delta\pi$, $1 h^{-1} \text{Mpc} \lesssim \Delta\pi \lesssim 2 h^{-1} \text{Mpc}$. The middle and right panels of Fig. 5 show the transmitted flux at separation $s \leq 0.5 h^{-1} \text{Mpc}$, $\bar{F}_0 = F(s < 0.5)$, as a function of the halo mass M assuming that all haloes with $M \geq 10^{11} M_\odot/h$ are surrounded with bubbles of radius $r_w = 0.5$ and $r_w = 1 h^{-1} \text{Mpc}$, respectively. As expected \bar{F}_0 is significantly larger for $r_w = 1 h^{-1} \text{Mpc}$. The dependence on halo mass appears to be stronger for $r_w = 1 h^{-1} \text{Mpc}$ than for $r_w = 0.5 h^{-1} \text{Mpc}$. In the former case, \bar{F}_0 decreases with increasing M by about $\Delta\bar{F}_0 = 0.20$ from $M = 10^{11}$ to $M = 10^{12} M_\odot/h$. This is consistent with the trend in the left panel which predicts that low mass haloes satisfy the condition $r_w \gtrsim (1+z)\sigma_v/H(z)$ more often than massive haloes as a result of the $\sigma_v - M$ dependence. For smaller bubbles, $r_w \lesssim 0.5 h^{-1} \text{Mpc}$, this appears to be rarely the case, independent of the mass of the halo.

To investigate the effect of the velocity field near haloes further we show the real space density and velocity field of the gas, as well as the absorption spectrum along two lines of sight passing haloes with $M = 2 \times 10^{11}$ (left panel) and $3 \times 10^{12} M_\odot/h$ (right panel) in Fig. 6. Solid and dotted line are for the case with and without wind bubbles, respectively. The radius of the bubbles is $r_w = 0.5 h^{-1} \text{Mpc}$ for both haloes. The difference between the two cases is striking. For the smaller mass halo in the left panel the flux level at the position of the halo is $\bar{F} \sim 0.9$ if the bubble is included whereas \bar{F} saturates at the redshift space position of the more massive halo in the right panel. Since the density fields

near the haloes in both panels show similar features, the difference in the flux values is mainly due to the difference in the velocity fields near the two haloes. The velocity shear in the less massive halo (left panel) is quite modest. On the contrary, the velocity field near the massive halo (right panel) has a large infall on a physical scale of a few hundred km s^{-1} , which moves some of the moderate density peaks close to the redshift space position of the halo. This effect occurs for a large fraction of haloes, and thereby reduces the overall expected \bar{F} at small scales by a few tens of percent.

5.3 The role of galaxy redshift error, LOS smoothing, and flux normalization

There is a number of other uncertainties which have to be taken into account when comparing the observed $F(s)$ with that calculated from the numerical simulation. Most important are the uncertain redshifts of the LBGs. There are large systematic shifts of several hundred km s^{-1} between the redshift of nebular emission lines, Ly α emission and interstellar absorption lines which make the assignment of a redshift somewhat ambiguous. ASSP give $\Delta z \geq 0.002$ or about 150 km s^{-1} as a typical error. We know however relatively little about the dynamical state of the responsible gas and there may well be larger systematic errors. The left panel of Fig. 7 shows the effect of adding a Gaussian distributed error to the redshift of the DM haloes. The solid curve shows the same model as the solid curve in the right panel of Fig. 3 (“massive” haloes, $r_w = 0.5 \text{ h}^{-1}\text{Mpc}$). Long-dashed and short-dashed curves are for redshift errors of $\sigma_z = 150 \text{ km s}^{-1}$ and 300 km s^{-1} , respectively. As expected introducing redshift errors smoothes out the large depression of the flux level at distances of up to $\sim 2 \text{ h}^{-1}\text{Mpc}$ to the line-of-sight. This substantially improves the agreement with the ASSP measurements on these scales.

In the middle panel of Fig. 7 the shaded area shows the 1σ error of the simulated $F(s)$ for our ensemble of LBG-size haloes with mass $M \geq 5 \times 10^{11} M_\odot/h$. The error-bars show the errors quoted by ASSP. To make the comparison easier the errors are plotted for the model with $\sigma_z = 150 \text{ km s}^{-1}$. The solid histogram shows the cumulative halo function $N(< s)$ (right axis) as a function of separation. At $s \leq 1 \text{ h}^{-1}\text{Mpc}$ the cumulative halo function $N(< s)$ is close to the cumulative galaxy function N_{LBG} of the ASSP sample, with $N(s < 0.5) = 3$ and $N(s < 1) = 11$ (resp. 3 and 12 in the ASSP sample). Our errors are generally larger than that of ASSP, at $s \leq 0.5 \text{ h}^{-1}\text{Mpc}$ by about 30 percent. At larger scales the difference is smaller but note that there our sample is about 20% larger than that of ASSP. Note also that the errors decrease faster than those of the transverse correlation $F(0, \sigma)$.

The mean flux level of QSO spectra varies significantly from spectrum to spectrum (10-20 percent). We thus also investigated how \bar{F} depends on the value of the mean flux $\langle F \rangle$. In the right panel of Fig. 7 we show the effect of varying $\langle F \rangle$. The long-dashed curve is our fiducial “massive” haloes model, which has $r_w = 0.5 \text{ h}^{-1}\text{Mpc}$ and $\sigma_z = 150 \text{ km s}^{-1}$. The upper (solid) and lower (short-dashed) curves show $\langle F \rangle = 0.72$ and 0.62 respectively. A larger (lower) mean

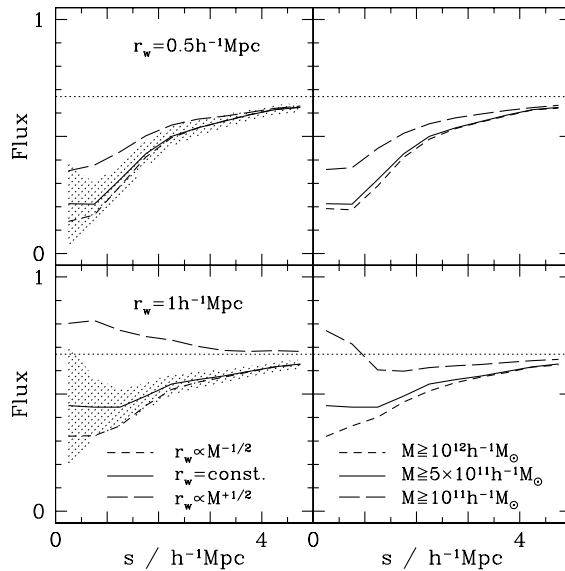


Figure 8. *Panels to the left* : $\bar{F}(s)$ for a mass-dependent r_w as indicated in the figure. Panels on the top row have $r_w = 0.5 \text{ h}^{-1}\text{Mpc}$, whereas panels on the bottom row have $r_w = 1 \text{ h}^{-1}\text{Mpc}$. The horizontal dotted line shows the mean flux, $\langle F \rangle = 0.67$. *Panels to the right* : the mean transmitted flux $\bar{F}(s)$ for three values of the halo mass limit M_{min} . The shaded area is the 1σ error, attached to the model $r_w = \text{const.}$

transmitted flux $\langle F \rangle$ raises (lowers) $\bar{F}(s)$ almost linearly by the same amount $\Delta F = \pm 0.05$ at all separations. $\langle F \rangle = 0.67$ matches the large scale ASSP measurements best.

5.4 The effect of varying the bubble model

5.4.1 \bar{F} with halo-mass dependent bubble size

So far we have considered bubbles with sizes that are independent of mass. Unfortunately, it is far from obvious what scaling with mass is appropriate. Obviously, on average more stars and a larger total energy input from stellar feedback are expected in the more massive haloes. However, simple binding energy arguments show that winds should escape more easily from low mass haloes (Larson 1974, Dekel & Silk 1986). This may be properly taken into account by a constant bubble radius but this is very uncertain. We therefore investigate the effect of different power-law scalings of the bubble size with mass. The left panels of Fig. 8 compare the case of constant bubble size with those assuming a power-law relation $r_w(M) \propto M^\nu$ with $\nu = +1/2$ and $-1/2$, at the minimal halo mass $M_{\text{min}} = 5 \times 10^{11} M_\odot/h$. The top panels are for $r_w = 0.5$ and the bottom panels are for $r_w = 1.0$. For $\nu = +1/2$ $\bar{F}(s)$ is very sensitive to the value of r_w and the mean flux at $s < 1 \text{ h}^{-1}\text{Mpc}$ rises to values as large as $\bar{F} = 0.8$ for the larger of the two bubble sizes improving the agreement with the results of ASSP. However, this is at the cost of the good agreement with the data on larger scales. It appears thus difficult to reproduce the observations of ASSP at small and large scales simultaneously by changing the mass-radius relation of the bubbles.

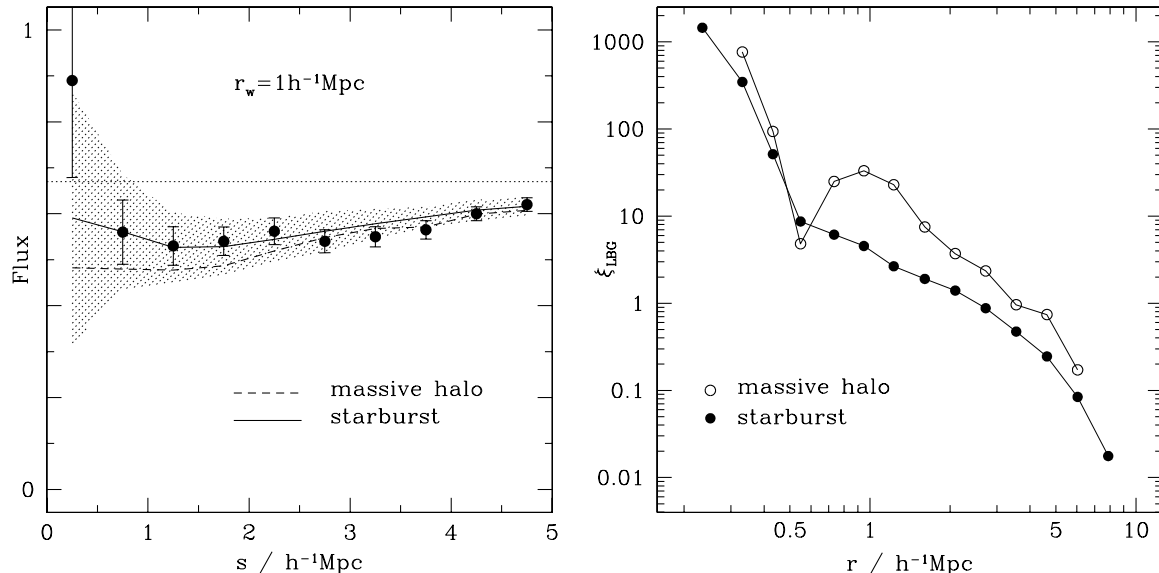


Figure 9. *Left panel* : Comparison between the “massive-halo” picture (dashed curve) and the “starburst” picture (solid curve). The shaded area shows the 1σ error. A Gaussian deviate of variance $\sigma_v = 150 \text{ km s}^{-1}$ was added to the halo positions *Right panel* : A comparison between the (real space) two-point correlation function of LBGs haloes in the “starburst” and “massive-halo” models. The filled and empty circles show ξ_{LBG} in the “starburst” and “massive-halo” models respectively. On comoving scale $r \sim 0.5 - 5 h^{-1}\text{Mpc}$, ξ_{LBG} in the “starburst” model follows a power-law of index $\gamma = 1.6$ and correlation length $r_0 = 2.5 h^{-1}\text{Mpc}$.

In the right panels of Fig.8 we investigate the effect of changing the minimum mass above which DM haloes are assumed to be surrounded by wind bubbles. Changing M_{min} will change the total space density of the halo as given in Table 2. There is less absorption if M_{min} decreases, mainly as a result of the increasing bubble filling factor. With a bubble radius $r_w = 1 h^{-1}\text{Mpc}$, the filling factor is $f_{\text{HII}} \sim 15\%$ and $\sim 1\%$ for $M \geq 10^{11}$ and $M \geq 10^{12} M_{\odot}/h$, respectively.

5.4.2 The starburst model

So far we have assumed that LBGs are hosted by the most massive haloes available and have introduced a minimum mass to match their space density with that observed for LBGs. This assumes that LBGs are long-lived and have the same brightness over a fair fraction of the Hubble time. This picture may be in conflict with the lack of the evolution of the space density of bright LBGs towards very high redshift which is more easily explained if LBGs are starbursts with a duty cycle of high star formation rate of less than 10%. This would mean that there is an about a factor ten or more larger number of DM haloes needed to host these LBGs than in the massive halo picture and the DM haloes hosting LBGs are less massive on average. As should be apparent from the previous section, for a given bubble size surrounding a typical LBG halo, this should reduce the effect of the velocity shear. It is then easier to reproduce the high mean flux levels at small separation. We investigate this alternative “starburst” picture here in more detail. Kolatt *et al.* (1999) developed a simple, *ad hoc* procedure to assign LBGs to colliding haloes identified in their N-body simulation and were able to reproduce both the number density and clustering properties of LBGs. Here, we will do something simpler and randomly

select haloes with mass $M \geq 10^{11} M_{\odot}/h$ such that their number density matches the observed LBGs number density, $n_{\text{LBG}} \sim 0.004 h^2\text{Mpc}^{-3}$. This corresponds to a duty cycle of ten percent. Note that only 10% of the haloes with a mass above $10^{11} M_{\odot}/h$ are haloes as massive as our “massive-halo” picture i.e. have masses $M \geq 10^{12} M_{\odot}/h$ (cf. Table 2). Most of the LBG-size haloes have $M \lesssim 5 \times 10^{11} M_{\odot}/h$ in the “starburst” scenario. We have produced 120 different Monte-Carlo realizations of such catalogs of starbursting haloes. In the left panel of Fig. 9 we compare $\bar{F}(s)$ for the “massive-halo” model (solid curve) and the “starburst” picture (dashed curve). For both we assume a bubble radius $r_w = 1 h^{-1}\text{Mpc}$ and a redshift error of the halo position of $\sigma_z = 150 \text{ km s}^{-1}$. At $s \lesssim 1 h^{-1}\text{Mpc}$ $\bar{F}(s)$ is larger in the “starburst” model by about 20%. We also plot the 1σ error for the starburst model and the ASSP measurements. Our starburst model with $r_w = 1 h^{-1}\text{Mpc}$ and a volume filling factor of 2% appears to be fully consistent with the ASSP measurement. Even at $s \lesssim 0.5 h^{-1}\text{Mpc}$, where our estimate of the cosmic variance error is 30% larger than that of ASSP, $\bar{F}(s)$ in the starburst model is only slightly more than 1σ below the ASSP measurement despite a difference in the mean flux of $\Delta\bar{F}(s) = 0.3$. Note that for the quoted volume filling factor we did only take into account the bubbles around the haloes that host LBGs at a given time. If the bubbles last longer than the LBG phase the volume filling factor would be higher by the same factor.

5.4.3 The clustering of LBG haloes

As discussed above our procedure to identify the host haloes of LBGs in the starburst model is rather crude. Unlike Kolatt *et al.* (1999) and Wechsler *et al.* (2001) we do not iden-

tify “colliding” haloes but choose a fraction of less massive haloes at random. It is thus not obvious that the host haloes chosen in this way will reproduce the clustering properties of LBGs. In the right panel of Fig. 9 we compare the two-point correlation function of our “starburst” and “massive-halo” models. The correlation function in the starburst model was computed from 120 different Monte-Carlo realizations of catalogs of starbursting haloes. The correlation lengths for the “starburst” and “massive-halo” models are $2.5 \text{ h}^{-1}\text{Mpc}$, and $3.5 \text{ h}^{-1}\text{Mpc}$, respectively. The observed correlation length is $r_0 \gtrsim 3 - 4 \text{ h}^{-1}\text{Mpc}$ (Adelberger *et al.* 1998, Adelberger 2000, Arnouts *et al.* 1999, Giavalisco & Dickinson 2001). The massive halo picture is thus in somewhat better agreement. However, the difference is small and as discussed above, Kolatt *et al.* (1999) and Wechsler *et al.* (2001) find that they can reproduce the observed clustering properties if they select “colliding haloes” as host galaxies of starbursting LBGs. We thus do not investigate this issue any further here.

5.5 Cosmic Variance

To understand better why the cosmic variance error becomes so large at small separation we plot the probability distribution $P(\bar{F}_0)$ in Fig. 10. The distribution is very broad. About 40% of the haloes have \bar{F}_0 larger than 0.8. The probability of finding three (uncorrelated) haloes with $\bar{F} \geq 0.8$ at separation $s \leq 0.5 \text{ h}^{-1}\text{Mpc}$ is thus still $\sim 5\text{-}10\%$. The symbols at the bottom of Figure 5 show the increase of \bar{F}_0 if the thermal motions and the velocity shear are artificially reduced by a factor of two. The broad probability distribution also explains why the suggestion of Croft *et al.* (2002) that LBGs are preferentially located in haloes with a low-density environment has such a strong effect on the mean transmission.

6 DISCUSSION

We used mock spectra obtained from numerical simulations to investigate the effect of fully ionised bubbles around the galactic haloes hosting LBGs on the H α distribution in the IGM as probed by the Ly α forest in QSO spectra. By matching the probability distribution and the power spectrum of the flux of mock spectra obtained from a N-body simulation of a Λ CDM model with those of observed spectra we derive an upper limit of 10% on the volume filling factor of bubbles. We further considered the mean transmitted flux at a given distance from galactic haloes. To model the observational data we computed the mean transmitted flux \bar{F} from an annular average of the two-dimensional conditional flux $\bar{F}(\pi, \sigma)$, in the same way as done by Adelberger *et al.* (2003). As previous investigations we find that the observed decrease of the transmission at separation $1 \leq s \leq 5 \text{ h}^{-1}\text{Mpc}$ to a halo is well reproduced by the simulated spectra. It is due to the increased matter density around haloes. We further find that an increase of the transmissivity at the smallest separations $s \leq 0.5 \text{ h}^{-1}\text{Mpc}$ requires bubble radii of $r_w = 1 - 1.5 \text{ h}^{-1}\text{Mpc}$. This is two to three times larger than the separation at which the increase of the transmissivity is observed. As discussed by Kollmeier *et al.* 2003 this is because in redshift space the velocity shear of the

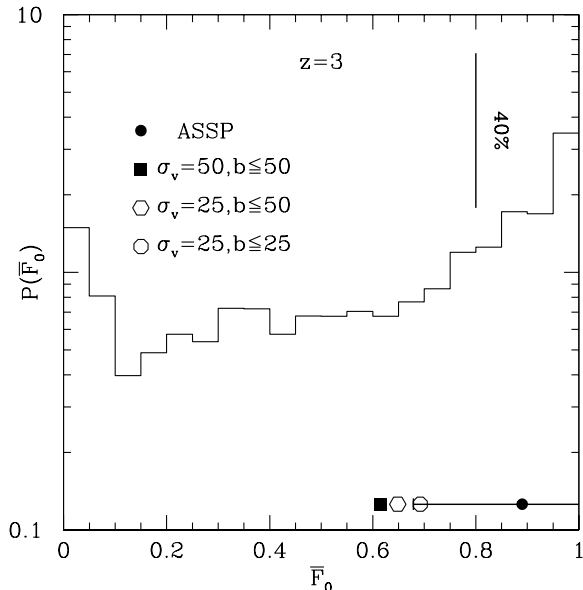


Figure 10. PDF of the transmitted flux at separation $s \leq 0.5 \text{ h}^{-1}\text{Mpc}$, \bar{F}_0 , in the “starburst” picture. The filled circle is \bar{F}_0 for $s \leq 0.5 \text{ h}^{-1}\text{Mpc}$ as quoted by Adelberger *et al.*, whereas the filled square is the “starburst” model. Empty symbols show \bar{F}_0 when the velocity shear and/or the Doppler parameter around haloes are reduced by a factor of two.

material infalling onto the halo fills in the cavity which is caused by the fully ionised wind bubble in real space. For a model where the haloes are surrounded with bubbles of size $r_w = 1 - 1.5 \text{ h}^{-1}\text{Mpc}$ there is no effect on either the flux PDF or the flux power spectrum. The flux PDF and the flux power spectrum of our simulated spectra are fully consistent with those of observed spectra. This is because the volume filling factor of the ionised bubbles is still small. We have investigated a variety of scalings of bubble size with halo mass. We also compared a model where LBGs are long-lived and are hosted by the most massive haloes with a model where LBGs are short-lived starbursts and are hosted by more numerous less massive haloes. Unlike Kolatt *et al.* (1999) and Wechsler *et al.* (2001), we do not identify starbursts as “colliding haloes” but choose a fraction of less massive haloes at random. Matching the observed transmission at scales $1 \leq s \leq 5 \text{ h}^{-1}\text{Mpc}$ is not difficult and there is certainly more than one way to do so. Introducing redshift errors at the expected level improves the agreement with the observations. The increase in transmission at small separation in our model spectra is, however, generally more gradual than that of the observed measurements. As other authors we found it challenging to match the observations at the smallest separation. Numerical simulations including galactic winds and simple analytical estimates as the one in Appendix A3 agree that the required bubble sizes are difficult to achieve (Croft *et al.* 2002, Bruscoli *et al.* 2002). We have thus particularly looked into models which are consistent with the observed measurements and are most “economical” in terms of bubble size. The velocity shear around haloes increases with increasing mass. Haloes of lower mass require thus smaller bubble radii to explain the observed increase of the transmission at $s \leq 0.5 \text{ h}^{-1}\text{Mpc}$. This may

favour a model where LBGs are starburst galaxies hosted by more numerous less massive haloes. We have taken special care in estimating the errors on the flux near galaxies in a similar way as done in the observations. For small separations we found that the expected error due to cosmic variance is about 30% larger than estimated by ASSP. Our starburst model is consistent with all measurements for a bubble radius of $r_w = 1 \text{ h}^{-1}\text{Mpc}$ and a volume filling factor of 2%. A bubble size of $r_w = 1 \text{ h}^{-1}\text{Mpc}$ appears, however, still difficult to achieve for galactic winds. If for some reason the velocity shear around haloes is smaller than suggested by our (DM only) simulation this would further reduce the required bubble size and filling factor. The correlation length for our “starburst” model is $2.5 \text{ h}^{-1}\text{Mpc}$, slightly lower than the observations. Identifying the LBGs with satellites infalling on high mass haloes, as in Kolatt *et al.* (1999), would further improve the agreement with the observed clustering properties of LBGs. However, this would be at the expense of matching the observed small-scale flux \bar{F} , since the velocity shear increases with halo mass. Therefore we advocate the model in which starbursts occur in small mass haloes. In a Λ CDM cosmology of normalisation $\sigma_8 = 0.9$, this model yields a reasonable match to the observed clustering of LBGs and transmitted flux \bar{F} . The mean transmitted flux of our simulated spectra at the smallest separation is 30 percent smaller than that of the ASSP sample. We would thus expect the observed mean transmission to decrease substantially for larger samples if the model is correct. A sample with 12 LBGs at separation $s \leq 0.5 \text{ h}^{-1}\text{Mpc}$ should reduce the error to $\Delta\bar{F} \sim 0.1$. This should help to discriminate against alternative models like the suggestion of Croft *et al.* (2002) that LBGs are located preferentially in low-density environments.

7 ACKNOWLEDGMENT

We acknowledge stimulating discussions with J. Primack and M. Pettini. We thank Juna Kollmeier, our referee, for constructive comments on the manuscript. This Research was supported by the Israel Science Foundation (grant No. 090929-1), the German Israeli Foundation for Scientific Research and Development, and the EC RTN network “The Physics of the Intergalactic Medium”. VD would like to acknowledge the MPA (Garching), the Institute of Astronomy (Cambridge) and the Technion Computing Center where part of this work was accomplished.

REFERENCES

- Adelberger K.L., Steidel C.C., Shapley A.E., Pettini M., 2003, ApJ, 584, 45
- Adelberger K.L., 2000, in ASP Conference Series, Vol. 200, Clustering at High Redshift, ed. A. Mazurek, O. Le Fèvre, V. Le Brun (Kluwer Academic Publisher)
- Adelberger K.L., Steidel C.C., Giavalisco M., Dickinson M., Pettini M., Kellogg M., 1998, ApJ, 505, 18
- Arnouts S., Cristiani S., Moscardini L., Matarrese S., Lucchin F., Fontana A., Giallongo E., 1999, MNRAS, 310, 540
- Bagla J.S., 1998, MNRAS, 299, 417
- Bahcall J.N., Salpeter E.E., 1965, ApJ, 142, 1677
- Bruscoli M., Ferrara A., Marri S., Schneider R., Maselli A., Rollinde E., Aracil B., 2003, MNRAS, 343, 41
- Bryan G.L., Machacek M., Anninos P., Norman M.L., 1999, ApJ, 517, 13
- Croft R.A.C., Hernquist L., Springel V., Westover M., White M., 2002, ApJ, 580, 634
- Davé R., Hernquist L., Katz N., Weinberg D.H., 1999, ApJ, 511, 521
- Dekel A., Silk J., 1986, ApJ, 303, 39
- Giavalisco M., Dickinson M., 2001, ApJ, 550, 177
- Gunn J.E., Peterson B.A., 1965, ApJ, 142, 1633
- Haehnelt M.G., Natarajan P., Rees M.J., 1998, MNRAS, 300, 817
- Heckman T.M., Armus L., Miley G.K., 1990, ApJS, 74, 833
- Heckman T.M., 2000, ASP Conf.Ser., 2000, 240, 345
- Heckman T.M., Lehnert M.D., Strickland D.K., Armus L., 2000, ApJS, 129, 493
- Hui L., Gnedin N.Y., 1997, MNRAS, 292, 27
- Katz N., Weinberg D.H., Hernquist L., 1996, ApJS, 105, 19
- Kolatt T.S., Bullock J.S., Somerville R.S., Sigad Y., Jonsson P., Kravtsov A.V., Kyplin A.A., Primack J.R., Faber S.M., Dekel A., 1999, ApJ, 345, 52
- Kollmeier J.A., Weinberg D.H., Davé R., Katz N., 2003a, ApJ, 594, 75
- Kollmeier J.A., Weinberg D.H., Romeel D., Katz N., 2003b, AIP Conf. Proc.666 191-194
- Larson R.B., 1974, MNRAS, 169, 229
- Lowenthal J.D., Koo D.C., Guzman R., Gallego J., Phillips A.C., Faber S.M., Vogt N.P., Illingworth G.D., Gronwall C., 1997, ApJ, 481, 673
- McDonald P., Miralda-Escude J., Rauch M., Sargent W.L.W., Barlow T.A., Cen R., Ostriker J.P., 2000, ApJ, 543, 1
- Ostriker J.P., McKee C.F., 1988, Rev. Mod. Phys., 60, 1
- Pettini M., Kellogg M., Steidel C.C., Dickinson M., Adelberger K.L., Giavalisco M., 1998, ApJ, 508, 539
- Pettini M., Shapley A.E., Steidel C.C., Cuby J.-G., Dickinson M., Moorwood A.F.M., Adelberger K.L., Giavalisco M., 2001, ApJ, 554, 981
- Rauch M., Miralda-Escude J., Sargent W.L.W., Barlow T.A., Weinberg D.H., Hernquist L., Katz N., Cen R., Ostriker J.P., 1997, ApJ, 489, 7
- Schaye J., Theuns T., Rauch M., Efstathiou G., Sargent W.L.W., 2000, MNRAS, 318, 817
- Sedov, L.I., 1959, “Similarity and Dimensional Methods in Mechanics”, (New-York:Academic)
- Shapley A.E., Steidel C.C., Adelberger K.L., Dickinson M., Giavalisco M., Pettini M., 2001, ApJ, 562, 95
- Sheth R.K., Tormen G., 1999, MNRAS, 308, 119
- Somerville R.S., Primack J.R., Faber S.M., 2001, MNRAS, 320, 504
- Springel V., Hernquist L., 2003, MNRAS, 339, 289
- Springel V., Yoshida N., White S.D.M., 2001, New Astronomy, 6, 79
- Steidel C.C., Giavalisco M., Dickinson M., Adelberger K., 1996, AJ, 112, 352
- Steidel C.C., Kollmeier J.A., Shapley A.E., Churchill C.W., Dickinson M., Pettini M., 2002, ApJ, 570, 526
- Stoehr F., White S.D.M., Tormen G., Springel V., 2002, MNRAS, 335, L84
- Sutherland R.S., Dopita M.A., 1993, ApJS, 88, 253
- Tegmark M., Silk J., Evrard A., 1993, ApJ, 417, 54
- Theuns T., Leonard A., Efstathiou G., Pearce F.R., Thomas P.A., 1998, MNRAS, 301, 478
- Theuns T., Schaye J., Haehnelt M.G., 2000, MNRAS, 315, 600
- Theuns T., Schaye J., Zaroubi S., Tae-Sun K., Tzanavaris P., Carswell B., 2002, ApJ, 567, 103
- Theuns T., Viel M., Kay S., Schaye J., Carswell R.F., Tzanavaris P., 2002, MNRAS, 578, 5

Trager S.C., Faber S.M., Dressler A., Oemler A., 1997, ApJ, 485, 92
 Weaver R., McCray R., Castor J., Shapiro P., Moore R., 1977, ApJ, 218, 377
 Wechsler R.H., Somerville R.S., Bullock J.S., Kolatt T.S., Primack J.R., Blumenthal G.R., Dekel A., 2001, ApJ, 554, 85
 Weinberg D.H., Romeel D., Katz N., Kollmeier J., 2003, AIP Conf. Proc 666 157-169

APPENDIX A: EVOLUTION OF BUBBLES

To explain the lack of H I close to the haloes, the dilute, highly ionised bubble has to survive for a sufficiently long time. In this appendix we present general order of magnitude estimates of the wind/shock energetics, relate that to the observed speeds, and estimate cooling time scales. We heavily rely on the work of Sedov (1959), Weaver *et al.* (1977), Ostriker & McKee (1988) and Tegmark *et al.* (1993).

A1 Wind energetics

The main characteristics of the wind, such as the temperature of the inner plasma, the size r_w of the bubble swept up by the shock and the wind velocity v_w , depend on the total energy E_w released in the outflow. Neglecting energy losses E_w can be estimated as

$$E_w = \frac{1}{2} M_w v_w^2 \quad (\text{A1})$$

$$\sim 4.3 \times 10^{56} \text{ erg} \left(\frac{r_w}{0.1 \text{ h}^{-1} \text{ Mpc}} \right)^3 \left(\frac{v_w}{100 \text{ km s}^{-1}} \right)^2 \Delta_g,$$

where M_w is the gas mass inside r_w . To get the numerical estimation we have assumed that $M_w = (4\pi/3)r_w^3 \rho_b \Delta_g$ where ρ_b is the mean background density and Δ_g is the density contrast inside r_w . The characteristic radius r_w and velocity v_w of the wind are poorly constrained, but recent observations suggest that $r_w \gtrsim 0.1 \text{ h}^{-1} \text{ Mpc}$ and $v_w \gtrsim 100 \text{ km s}^{-1}$ (Heckman *et al.* 2000, Pettini *et al.* 2001, Adelberger *et al.* 2003). On scales $r \sim 0.1 \text{ h}^{-1} \text{ Mpc}$ the value of Δ_g is typically about 2–5, which gives $E_w \sim 10^{57} \text{ erg}$. This value is consistent with the amount of energy E_{SN} released by supernovae during a burst of duration $t_{burst} \sim 10^7 \text{ yr}$ and of star formation rate $\dot{M}_* \sim 10 M_{\odot} \text{ yr}^{-1}$.

To assess whether the gas will be expelled from the halo one can apply a simple binding argument (e.g. Dekel & Silk 1986). On the one hand the potential energy U of the gas which lies within the halo is $U \propto M M_g / r_M$, where r_M is the characteristic radius of the halo, $r_M \propto M^{1/3}$, and M_g is the mass of the gas which lie within a radius r_M . The mass of the gas in the halo is $M_g \propto f_* f_b M$, where f_* is the star formation efficiency and f_b the average fraction of baryons in the halo. The potential energy is then $U \propto M^{5/3}$. On the other hand, if one assumes that winds are driven by supernovae, the energy released in the wind is $E_w \propto \dot{M}_* t_{burst}$, where $\dot{M}_* \propto M_g$ is the star formation rate. Hence, according to this crude estimate, the ratio of the kinetic to binding energy is $E_w / U \sim M^{-2/3}$. We therefore expect r_w to be a function of M , and outflows to escape more easily from low mass haloes (e.g. from dwarf galaxies). On this

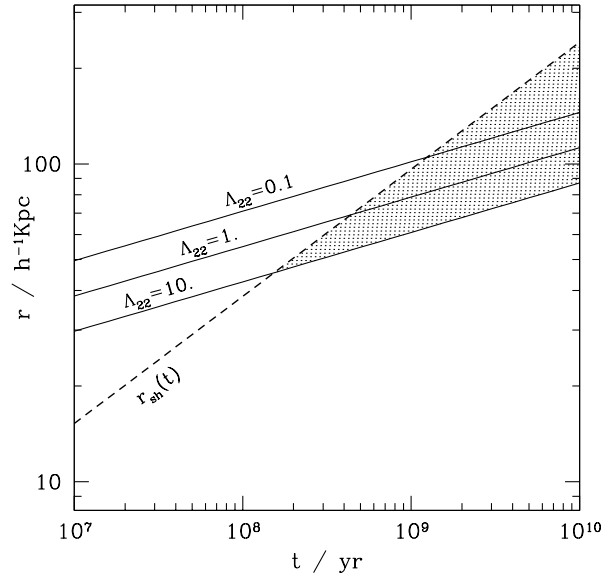


Figure A1. The cooling radius $r_{cool}(t)$ (solid curves) for various cooling time rate. The dashed curve is $r_{sh}(t)$.

latter point, the measurements of Adelberger *et al.* (2003) seem to indicate that, if outflows are the cause of lack of H I absorption in the observed transmitted flux \bar{F} , they can escape from high mass galaxies as well, and affect the IGM properties on comoving scale as large as $0.5 \text{ h}^{-1} \text{ Mpc}$.

A2 Propagation of adiabatic shock

A wind ejects energy in the IGM, driving a shock which heats up and collisionally ionises the material it encounters. We briefly review now the evolution of the shock front and the ionised bubble it encompasses, before radiative losses become important. We assume that the gas follows the perfect gas law $P = (\gamma - 1)u\rho$, where P , u and ρ are, respectively, the pressure, the internal energy and the density of the gas, and γ is the ratio of specific heats, which is $\gamma = 5/3$ for a mono-atomic gas. If the expansion of the universe can be ignored, the shock is well described by a strong adiabatic blast wave which propagates into the IGM. In this regime, accurate self-similar solutions exist. Let $r_{sh}(t)$ be the position of the shock front at time t after the burst. The jump conditions relate the density ρ_{IGM} of the unperturbed IGM to the density ρ_{sh} , the pressure P_{sh} and the temperature T_{sh} at the shock front. For a strong adiabatic shock the jump conditions for pressure and density can be expressed as

$$\rho_{sh} = \frac{(\gamma + 1)}{(\gamma - 1)} \rho_{IGM}, \quad P_{sh} = \frac{2}{\gamma - 1} \rho_{IGM} \frac{dr_{sh}}{dt}^2. \quad (\text{A2})$$

Hence, $\rho_{sh} = 4\rho_{IGM}$ for an adiabatic index $\gamma = 5/3$. Assuming that the flow is self-similar, r_{sh} can be expressed as a function of the similarity variable ξ . The position of the shock front corresponds then to a fixed value of $\xi \simeq 1$. Hence, r_{sh} is given by (Sedov 1959)

$$r_{\text{sh}} = \left(\frac{E_w}{\rho_{\text{IGM}}} \right)^{1/5} t^{2/5}, \quad (\text{A3})$$

where $E_w \sim 10^{57}$ erg is the energy released in the wind. Inserting the value of E_w in the expressions of r_{sh} and T_{sh} , we find

$$r_{\text{sh}}(t) \simeq 19 \text{ h}^{-1} \text{ kpc} \left(\frac{t}{10^7 \text{ yr}} \right)^{0.4} \quad (\text{A4})$$

$$T_{\text{sh}}(t) \simeq 2.7 \times 10^7 \text{ K} \left(\frac{t}{10^7 \text{ yr}} \right)^{-1.2} \quad (\text{A5})$$

$$\frac{1}{\Delta_g^{0.2}} \left(\frac{\Omega_b h^2}{0.019} \right)^{-0.2} \left(\frac{E_w}{10^{57} \text{ erg}} \right)^{0.2} \left(\frac{1+z}{4} \right)^{-0.6}$$

$$\frac{1}{\Delta_g^{0.4}} \left(\frac{\Omega_b h^2}{0.019} \right)^{-0.4} \left(\frac{E_w}{10^{57} \text{ erg}} \right)^{0.4} \left(\frac{1+z}{4} \right)^{-1.2}$$

Since the temperature behind the shock front $T \propto P/\rho$ is a decreasing function of r , T reaches its minimum at the shock front. This solution holds only in the regime where the expansion is negligible, i.e. $t \ll t_H$ where t_H is the Hubble time scale. Self-similar solutions for $t > t_H$ including this latter complication exist (Ostriker & McKee 1988), but since energy and momentum conservation break down for $t \sim t_H$, it is difficult to express the asymptotic solution as a function of the initial E_w .

A3 Cooling time-scales and survival of bubbles

The evolution of such an expanding shock depends critically on cooling which will lower the temperature of the shell and its interior, thereby increasing the amount of H I hydrogen available for Ly α resonant scattering. The expanding shell cools due to radiative losses. The shock will undergo a phase of shell formation which will occur when the energy dissipated in a volume $\propto r_{\text{sh}}(t)^3$ will be of the order of E_w .

Cooling is expected to be more efficient at the shock front since, at $r = r_{\text{sh}}$, the density (temperature) is larger (lower) than at $r < r_{\text{sh}}$. Thus, shell formation first occurs at the shock front. As long as we are in the regime of low density, $\rho \ll \rho_{\text{IGM}}$, and high temperature, $T \gg 10^6$ K, radiative cooling is dominated by thermal bremsstrahlung. However, for temperature $T \lesssim 10^6$ K, atomic line cooling might contribute significantly to the cooling rate Λ (in $\text{erg cm}^3 \text{ s}^{-1}$) if the wind is enriched with heavy elements. For a wind of metallicity $Z \sim 0.1 Z_\odot$ (e.g. Adelberger *et al.* 2003), the cooling rate is $\Lambda \sim 10^{-22}$ erg in the range $10^4 \lesssim T \lesssim 10^6$ K (e.g. Sutherland & Dopita 1993).

We assume that cooling at the shock front, where the temperature is $T \lesssim 10^6$ K, is dominated by atomic line transitions. This is true when the temperature of the shell is $T_{\text{sh}} \lesssim 10^6$ K, i.e. for times $t \gtrsim 10^8$ yr. The cooling time scale at the shock front is then $t_{\text{cool}}(r_{\text{sh}}, t) = 3k_B T_{\text{sh}} / (2n_{\text{sh}} \Lambda)$,

$$t_{\text{cool}}(r_{\text{sh}}, t) = 1.9 \times 10^{10} \text{ yr} \left(\frac{t}{10^7 \text{ yr}} \right)^{-1.2} \Lambda_{22}^{-1}$$

$$\frac{1}{\Delta_g^{1.4}} \left(\frac{\Omega_b h^2}{0.019} \right)^{-1.4} \left(\frac{E_w}{10^{57} \text{ erg}} \right)^{0.4} \left(\frac{1+z}{4} \right)^{-4.2}$$

where the cooling rate Λ_{22} is in unit of $10^{-22} \text{ erg cm}^3 \text{ s}^{-1}$ and is assumed to be constant in the temperature range $10^4 \lesssim T_{\text{sh}} \lesssim 10^6$ K.

Once the shell starts forming, the temperature T_{sh} of the shell cools to $\sim 10^4$ K on a very short time scale. However, in the range $T \lesssim 10^4$ K, the cooling rate Λ drops sharply from $\sim 10^{-22}$ down to $\sim 10^{-26} \text{ erg cm}^3 \text{ s}^{-1}$ (Sutherland & Dopita 1993) and the shell cannot cool below temperature $T \sim 10^4$ K. We define now a radius $r_{\text{cool}}(t)$ such that the cooling time scale t_{cool} as a function of radius r satisfies $t_{\text{cool}} < t$ for $r > r_{\text{cool}}$. According to this definition, the gas between $r_{\text{cool}}(t)$ and $r_{\text{sh}}(t)$ has cooled onto the shell by the time t . To express t_{cool} as a function of r and t , it should be noted that the number density $n_w(r, t)$ behind the shock front (in cm^{-3}) scales as $n_w(r, t) = (r/r_{\text{sh}})^\alpha n_{\text{sh}}(t)$ with $\alpha \sim 4.5$ typically. This relation is however valid in the asymptotic regime only. Therefore, assuming that the plasma has reached pressure equilibrium, the temperature $T_w(r, t)$ behind the shock front is $T_w = (r_{\text{sh}}/r)^\alpha T_{\text{sh}}$, and the radiative cooling time scale t_{cool} is

$$t_{\text{cool}}(r, t) = \left(\frac{r_{\text{sh}}}{r} \right)^{2\alpha} t_{\text{cool}}(r_{\text{sh}}, t). \quad (\text{A7})$$

On Fig. A1 the solid curves are $r_{\text{cool}}(t)$ for various cooling time rate Λ_{22} , and the dashed curve is $r_{\text{sh}}(t)$. The shell starts forming at the shock front when $r_{\text{cool}}(t)$ intersects $r_{\text{sh}}(t)$. For larger time, cooling occurs for $r_{\text{cool}}(t) < r < r_{\text{sh}}(t)$ (shaded area). Since most of the gas swept up by the wind lies at $r \lesssim r_{\text{sh}}$, a large fraction of gas cools down to $T \sim 10^4$ K shortly after the shell formation. For $\Lambda_{22} = 1$, about 30% of the mass enclosed in the bubble has cooled into the shell over a Hubble time t_H , where $t_H \simeq 1.2 \times 10^9 (\Omega_m h^2)^{-1/2}$ at $z = 3$. For a high metallicity wind $Z \gtrsim 0.1 Z_\odot$, cooling becomes severe for $t \gtrsim$ a few 10^8 yr, a time scale shorter than the Hubble time scale t_H at $z = 3$. On the contrary, for a low metallicity wind, $Z \ll 0.1 Z_\odot$, the cooling rate is $\Lambda_{22} \ll 1$ and cooling will not become significant for $t \lesssim t_H$. Hence, most of the bubbles will not survive over a Hubble time scale unless the cooling time rate Λ_{22} , or the wind metallicity Z , is very low. For radii $r \lesssim r_{\text{cool}}(t)$, the temperature is higher than 10^6 K, and thermal bremsstrahlung and inverse Compton cooling prevail over line cooling, but the corresponding cooling times are still smaller than the Hubble time at $z = 3$.

A4 Absorption by the cold shell

To compute the thickness $\Delta s(t)$ of the shell, we assume that the pressure is constant through the inner plasma and the shell. Since the temperature of the shell, $T_{\text{sh}} \sim 10^4$ K, is much lower than the overall temperature $T_w \gtrsim 10^6$ K of the highly ionised plasma, we expect $\Delta s(t) \ll r_{\text{sh}}(t)$, i.e. the shell is thin. Taking into account this assumption, we find

$$(\text{A6}) \frac{\Delta s}{r_{\text{sh}}} = \frac{1}{3} \left(\frac{T_{\text{sh}}}{T_w} \right) \left[1 - \left(\frac{r_{\text{cool}}}{r_{\text{sh}}} \right)^3 \right], \quad (\text{A8})$$

a result consistent with a thin shell approximation. Assuming $T_w = 100 T_{\text{sh}} = 10^6$ K and neglecting the expansion of

the Universe gives $\Delta s \lesssim 0.01 r_{\text{sh}}$. Δs should thus not exceed a few $h^{-1}\text{kpc}$, a scale which cannot be resolved in our simulation. The optical depth for resonant Ly α scattering is given by

$$\begin{aligned} \tau &\sim \sigma_0 n_{\text{sh}} \Delta s & (\text{A9}) \\ &\sim 1.6 \eta \Delta_g \left(\frac{\Omega_b h^2}{0.019} \right) \left(\frac{1+z}{4} \right)^2 \left(\frac{r_w}{0.1 h^{-1}\text{Mpc}} \right), \end{aligned}$$

where $\eta \simeq 1$ is the H I neutral fraction at temperature $T \sim 10^4 \text{K}$. Ly α absorption is expected for reasonable values of the density contrast $\Delta g \sim 2-3$, the typical comoving radius of the bubble $r_w \sim 0.1 h^{-1}\text{Mpc}$, and the baryon fraction $\Omega_b h^2 \sim 0.02$. However, since we cannot resolve the thin shell in our simulation, we have nevertheless ignored its Ly α absorption.

APPENDIX B: NUMERICAL CONVERGENCE

To assess the sensitivity of the transmitted flux to numerical resolution, we perform a calculation with the highest resolution simulation of the series, which has a mass resolution $m = 1.66 \times 10^8 M_\odot/h$. The halo catalog and the flux in the simulation are computed as in Section §3 with a pixel resolution $\Delta = 60 h^{-1}\text{kpc}$ (comoving). We added a Gaussian deviate of variance $\sigma_v = 150 \text{km s}^{-1}$ to the halo positions. In Fig. B1 we show the transmitted flux as computed in the “starburst” scenario for a bubble radius $r_w = 1 h^{-1}\text{Mpc}$. The mass resolution is $m = 9.52$ (dashed curve) and $m = 1.66 \times 10^8 M_\odot/h$ (solid curve). In the latter the strong absorption lines are better resolved, thereby slightly reducing the normalization of the optical depth \mathcal{A} . Therefore, the optical depth of the absorbing material is lower, and the transmitted flux is slightly larger, by about $\Delta \bar{F} \sim 0.02$ on scales of $2 \leq s \leq 4 h^{-1}\text{Mpc}$.

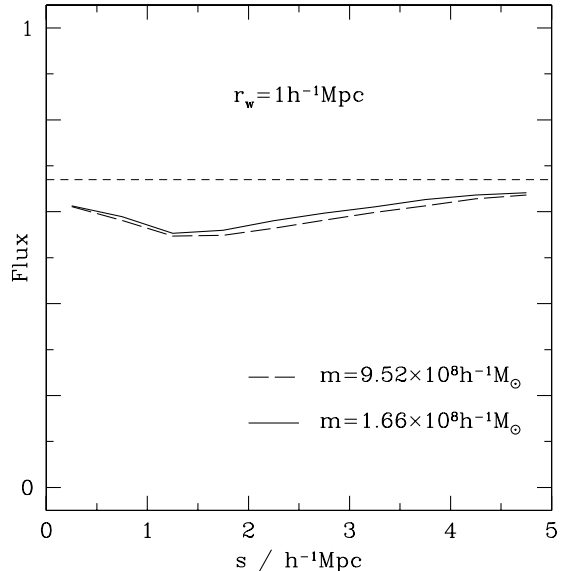


Figure B1. The transmitted flux \bar{F} in the “starburst” scenario with bubbles of radius $r_w = 1 h^{-1}\text{Mpc}$, with DM particle mass resolution $m = 9.52 \times 10^8$ (dashed curve) and $1.66 \times 10^8 M_\odot/h$ (solid curve). The horizontal dashed line is the flux normalization, $\langle F \rangle = 0.67$.